

Using nonequilibrium thermodynamics to optimize the cooling of a dilute atomic gas

Daniel Mayer,¹ Felix Schmidt,¹ Steve Haupt,¹ Quentin Bouton,¹
 Daniel Adam,¹ Tobias Lausch,¹ Eric Lutz,² and Artur Widera^{1,3}

¹*Department of Physics and Research Center OPTIMAS, Technische Universität Kaiserslautern, Germany*

²*Institute for Theoretical Physics I, University of Stuttgart, D-70550 Stuttgart, Germany*

³*Graduate School Materials Science in Mainz, Gottlieb-Daimler-Strasse 47, 67663 Kaiserslautern, Germany*

Optimizing thermodynamic processes far from equilibrium is a challenge. We report the experimental optimization of cooling and thermalization of a gas of few noninteracting Cesium atoms confined in a nonharmonic optical dipole trap. To this end, we combine degenerate Raman sideband cooling and nonequilibrium thermodynamics. We determine the axial phase-space distribution of the atoms after each Raman cooling pulse by tracing the evolution of the gas with position-resolved fluorescence imaging. We further minimize the entropy production to a target thermal state to specify the optimal spacing between a sequence of pulses, thus achieving optimal thermalization. We finally study the dynamics of the cooling process by measuring the statistical distance between each cooling step. Our results provide a method to systematically optimize the cooling of nonharmonically trapped dilute gases and illustrate the power of nonequilibrium thermodynamics.

A primary objective of thermodynamics is to optimize processes. Optimization goals vary depending on the application: they include the minimization of dissipation as well as the maximization of work output or of cooling power [1]. For macroscopic systems, the properties of optimal transformations have been studied in detail within finite-time thermodynamics [2–5]. The two central quantities of this approach are the entropy production and the thermodynamic length which measures the distance from equilibrium at which a system operates. Both are calculated in the linear response regime by expanding thermodynamic potentials, such as entropy or internal energy, to lowest order around their equilibrium values [2–5]. These techniques have been employed to optimize fractional distillation and other thermodynamic processes [2–7]. For microscopic systems, such as colloidal particles, where thermal fluctuations are sizable, this optimization framework has been successfully extended to the level of individual trajectories within stochastic thermodynamics [8–11]. In particular, methods to theoretically compute and experimentally evaluate the thermodynamic length have been proposed [19–22]. While the nonequilibrium entropy production has been measured in a number of experiments [12–18], the thermodynamic distance has yet to be determined experimentally.

A central assumption of both finite-time and stochastic thermodynamics is that systems are coupled to ideal heat baths that induce full phase-space thermalization. However, this hypothesis is often not fulfilled at the atomic level. A prominent instance is provided by laser cooling of atoms which plays an essential role in the study of new states of matter and high-resolution spectroscopy [24]. Most laser cooling schemes only induce thermalization of the momentum degrees of freedom [23]. In dense atomic samples, frequent atomic collisions redistribute the energy and establish thermal equilibrium. By contrast, in dilute gases with rare interparticle collisions, these non-ideal reservoirs lead to far from equilibrium states. Their

description thus lies outside the currently existing framework. New experimental and theoretical tools are therefore required to achieve their thermalization.

We here report the optimization of subrecoil cooling of a dilute gas of Cesium atoms, confined in an optical dipole trap [23], using degenerate Raman sideband cooling (DRSC) [25–27]. This technique is a standard subrecoil cooling scheme for a variety of atomic systems [28–37]. In our experiment, short pulses of Raman cooling lasers are applied to an initially thermal cloud along the axial direction of the nonharmonic trap. Axial and radial directions are only weakly coupled, making the problem essentially one-dimensional. The Raman pulses thermalize the atomic momentum to the Raman temperature but leave the position distribution unchanged, thus creating a nonequilibrium state which does not thermalize on its own. The nonharmonicity of the trap further leads to nontrivial dynamics.

In order to realize complete phase-space thermalization, we devise protocols consisting of a train of Raman pulses separated by intervals of free evolution (Fig. 1a). For concreteness, we consider a sequence of three equally spaced pulses. The first Raman pulse (RP1) decreases the energy of the gas and moves it out of equilibrium. The second and third pulses (RP2 and RP3) drive the gas back to a thermal state while cooling it further. We seek the optimal pulse spacing by minimizing the entropic distance to the equilibrium state at the Raman temperature. We obtain an overlap with the desired distribution of about 75% for the optimal spacing, more than twice the value for nonoptimal protocols. To this end, we use in-situ fluorescence imaging to characterize the effect of each Raman pulse by tracing the time evolution of the axial position distribution of the cloud (Figs. 1b-d) [38]. Combining these with numerical simulations, we determine the initial as well as the final (Raman) temperature. As a result, we are able to experimentally access the axial phase-space distribution of the atoms after

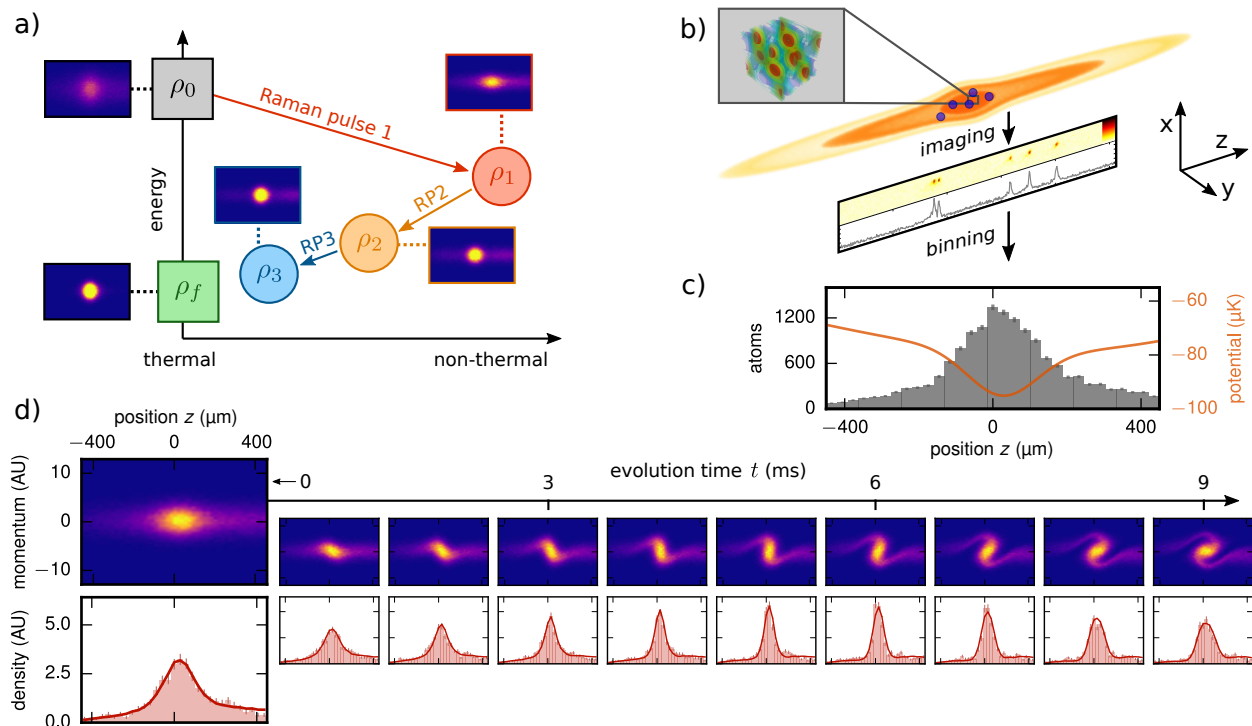


FIG. 1. Experimental setup. **a)** An initial thermal state ρ_0 of a noninteracting gas of Cs atoms is cooled and thermalized by a sequence of degenerate Raman sideband cooling pulses (red, orange and blue) with equal spacing, defining a cooling map. Each cooling pulse only thermalizes the momentum degree of freedom. The first cooling pulse thus creates a nonthermal state while the successive Raman pulses drive the system into the target thermal state ρ_f . **b)** The axial position distribution of the atoms confined in a crossed optical dipole trap is experimentally determined by employing fluorescence imaging in a one-dimensional optical lattice. The inset shows the pattern of the overlapped three-dimensional lattice of the Raman lasers. **c)** Initial position distribution (grey bars) with temperature $T_0 = 12.1(11)$ μK in the nonharmonic trapping potential (orange line). **d)** Simulated free time evolution of the phase-space and corresponding projected axial density distribution (red solid line). The comparison with experimental data (red bars) allows us to determine the Raman temperature $T_R = 2.9(2)$ μK .

each Raman pulse, which is given by the product of position and momentum marginals. We further theoretically define and experimentally determine the statistical distance between each pulse. The latter quantity extends the thermodynamic length to the present nonequilibrium situation. We find that optimal thermalization is mainly reached during the first two cooling stages.

We initialize our system by trapping an average of 7 Cs atoms from background vapor in a magneto-optical trap and transfer them into a crossed optical dipole trap which creates a conservative potential (Fig. 1b). The atomic collision rate of 36 Hz at peak density is smaller than the inverse evolution time used in the experiment. The cloud is thus effectively noninteracting. The initial thermal state at temperature T_0 is prepared by applying an optical molasses pulse [23]. We then extract the atomic positions along the axial z -direction by employing fluorescence imaging in a one-dimensional optical lattice [38] and obtain the experimental position distribution $f(z)$ after binning (Fig. 1c). Every measurement is repeated several hundred times with identical parameters in order

to get sufficient statistics. The dipole trap potential is approximately harmonic in radial direction (x, y) with trap frequency $\omega_r = 2\pi \times 1.1$ kHz. The potential is markedly anharmonic in the axial z -direction and the position distribution features pronounced wings (Figs. 1c-d). At the center of the trap, the harmonic approximation yields an axial frequency of $\omega_a = 2\pi \times 60$ Hz. In order to determine the initial temperature of the gas, we compare the measured position distributions $f(z)$ to numerical simulations of the atoms that take the full three-dimensional trapping potential into account for various temperatures [39]. Using a χ^2 -analysis [40], we find an initial temperature $T_0 = 12.1(11)$ μK [41].

We next cool the atomic cloud by applying a train of DRSC pulses with duration of 10 ms each, following the scheme of Ref. [26]. Details on our experimental setup may be found in Refs. [39, 42]. During the DRSC pulse, atoms are confined in a superposed 3D optical lattice created by the Raman lasers sketched in Fig. 1b. The lattice spacing is smaller than 1 μm , which is much less than the typical dimension of the cloud in the optical dipole trap.

The position distribution of the atoms in the dipole trap is therefore effectively frozen during the cooling pulse. At the same time, Raman processes reduce the vibrational quantum number of the atoms trapped in the Raman lattice, thus reducing their kinetic energy. Since the potential energy in the crossed dipole trap is unchanged, such a cooling pulse creates a nonthermal state. For the numerical simulations of the cooling protocol, all parameters are specified by independent measurements. The only remaining variable is therefore the Raman temperature T_R which we determine by monitoring the free evolution of the gas and comparing it with numerical simulations. We model the DRSC pulse by resetting the momenta with random values drawn from a Maxwell distribution at temperature T_R . We find $T_R = 2.9(2) \mu\text{K}$ [41]. An example of such a simulation is shown in Fig. 1d: while the axial phase-space distribution simply rotates in the two-dimensional space (z, p_z) for a harmonic trapping potential, we here observe the creation of whorls induced by the nonlinearity of the trap [49]. The projection onto the position axis shows excellent agreement between numerics and experimental data at all times.

For a nonequilibrium process from an initial thermal state ρ_0 at inverse temperature $\beta_0 = (k_B T_0)^{-1}$ to a final thermal state ρ_f at inverse temperature β_f , the (axial) Gibbs-Shannon entropy, $S = -\int dz dp_z \rho \ln \rho$, where $\rho = \rho(z, p_z)$ is the (axial) phase-space density, satisfies $\Delta S = S_f - S_0 = \beta_f Q + \Sigma$ [44–46]. Here, $Q = \int dz dp_z (\rho_f - \rho_0) H$ is the heat absorbed by the system, H its Hamiltonian and $\Sigma = D(\rho_0 || \rho_f) = \int dz dp_z \rho_0 \ln(\rho_0 / \rho_f)$ the entropy production given as the relative entropy between initial and final states [48]. For a discrete sequence of nonthermal intermediate states ρ_i , as created after each Raman cooling pulse in our experiment, the entropy production associated with each step i reads [41],

$$\Sigma_i = D(\rho_i || \rho_f) - D(\rho_{i+1} || \rho_f). \quad (1)$$

The square root of Eq. (1) defines a statistical length, $L_i = \sqrt{2\Sigma_i}$, that quantifies the system's distance from equilibrium. It reduces to the usual thermodynamic length in the limit of quasistatic processes where all the intermediate states are close to thermal [4–7].

Commonly considered optimization schemes minimize the entropy production with fixed initial and final states [4–7]. By contrast, the state ρ_3 after the last Raman pulse here depends on the entire cooling sequence and is hence not fixed. Our strategy is therefore to minimize the entropic distance to the target thermal state ρ_f and identify the final temperature with the Raman temperature, $\beta_f = \beta_R$. We concretely study two optimization criteria: The first (static) condition minimizes the relative entropy between ρ_3 and the target state ρ_f , $D(\rho_3 || \rho_f)$, in Eq. (1). Since the momentum distribution $\tilde{f}_i(p_z) = \tilde{f}_f(p_z)$ is randomized during each Raman pulse, it is independent from the position distribution

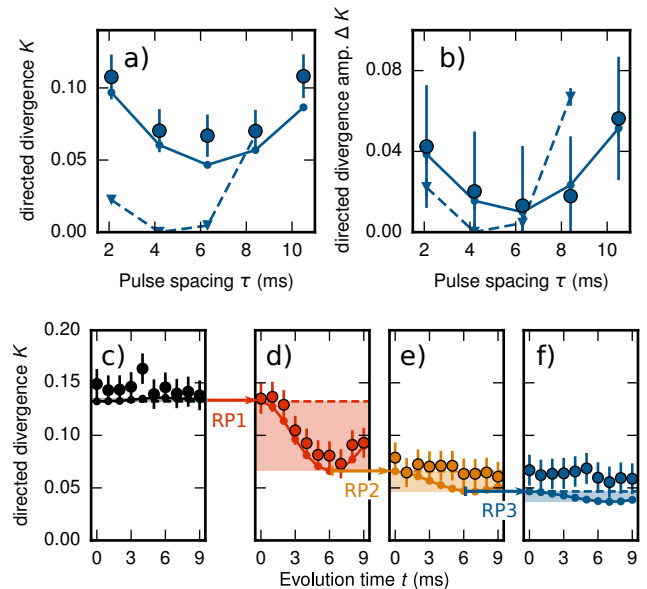


FIG. 2. Optimization criteria. **a)** Directed divergence $K(\rho_3 || \rho_f)$ between the state ρ_3 after the last Raman pulse and the target thermal state ρ_f for different pulse spacings: small triangles (dots) correspond to simulations of the harmonic (nonharmonic) trapping potentials and large dots show experimental data. **b)** Oscillation amplitude $\Delta K = \max_t K(f_3(t) || f_f) - \min_t K(f_3(t) || f_f)$ for the position distribution f_3 after the last cooling pulse and the target position distribution f_f for various pulse spacings. Both conditions yield an optimal spacing of 6.3 ms for the nonharmonic experimental trap and 4.2 ms for the harmonic trap. **c)-f)** Time evolution of oscillation amplitude ΔK after each Raman pulse for the optimal time 6.3 ms: no oscillations are seen for the initial thermal state (black), while they increase after the first cooling pulse (red), before decreasing again after each Raman pulse that lead to thermalization (orange and blue).

$f_i(z)$. As a result, the phase-space distribution factorizes $\rho_i(z, p_z) = f_i(z) \tilde{f}_f(p_z)$. Both marginals are determined from the experimental data. We thus have direct access to the full axial phase-space distribution $\rho_i(z, p_z)$ after each cooling pulse. Since the factorization property also holds true for a thermal state, we have $\rho_f(z, p_z) = f_f(z) \tilde{f}_f(p_z)$. The additivity of the relative entropy for independent distributions [48] then implies that the entropic distance between ρ_3 and the target state ρ_f simplifies to $D(\rho_3 || \rho_f) = D(f_3(z) || f_f(z)) + D(\tilde{f}_f(p_z) || \tilde{f}_f(p_z)) = D(f_3(z) || f_f(z))$. The second (dynamic) criterion minimizes the oscillations of the relative entropy, $\Delta D = \max_t D(f_3(t) || f_f) - \min_t D(f_3(t) || f_f)$, during the free time evolution of the atomic cloud after the last Raman pulse. This criterion is based on the stationarity of a thermal state: for an equilibrium state, the distribution f_3 is constant in time and hence $\Delta D = 0$. The closer the state is to equilibrium, the smaller the

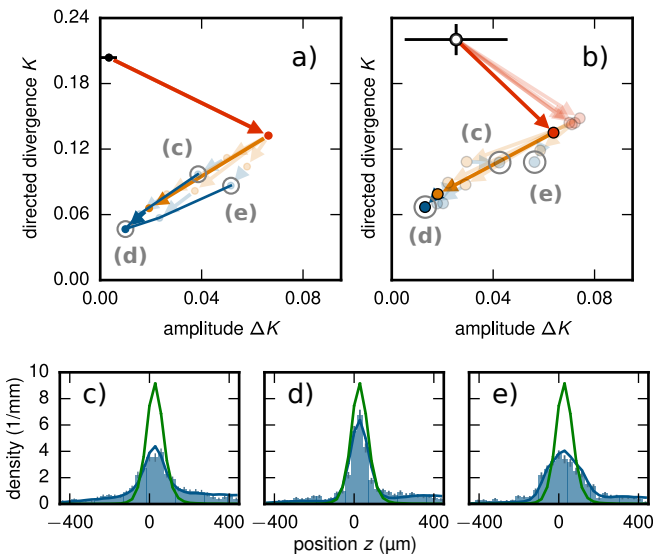


FIG. 3. Cooling map. **a)** Simulated cooling process in the plane $(K, \Delta K)$ of the two optimization quantities of Fig. 2. The initial thermal state is represented in black. The red, yellow and blue arrows visualize the effect of the individual cooling pulses. The last states for $\tau = 2.1$ ms, 6.3 ms and 10.5 ms are labeled with (c), (d) and (e). The blue line connects all last states, indicating the different cooling results of the protocols. **b)** Corresponding experimental cooling process. The hollow point includes the numerical contribution of the directed divergence of the momentum distribution [41]. **c-e)** Atom distributions after the last Raman pulse for $\tau = 2.1$ ms, 6.3 ms and 10.5 ms. The experimental distribution (blue bars) and the corresponding simulation (blue solid line) are shown with the simulated target distribution (green solid line) as a reference. An overlap of 75% is obtained for the optimal spacing d).

oscillation amplitude ΔD .

The practical implementation of the above optimization criteria faces the problem that the relative entropy is only well-defined for probability distributions that are absolutely continuous with respect to one another, that is, there is no point at which one distribution vanishes, while the other one does not [47]. Any occurrence of zero bins, due to finite statistics, in the experimentally measured or in the numerically simulated distribution in the denominator will thus result, for a nonvanishing numerator, in a division by zero [41]. We therefore replace in the following analysis the relative entropy by the closely related K directed divergence defined as $K(\rho_a||\rho_b) = D(\rho_a||(\rho_a + \rho_b)/2)$ [47]. The latter satisfies $K(\rho_a||\rho_b) \geq 0$ and $K(\rho_a||\rho_b) = 0$ if and only if $\rho_a = \rho_b$, like the relative entropy. Nonetheless it is always well defined irrespective of the values of ρ_a and ρ_b . It is further bounded by the relative entropy, $K(\rho_a||\rho_b) \leq D(\rho_a||\rho_b)/2$ [47].

Figure 2a presents the implementation of the first opti-

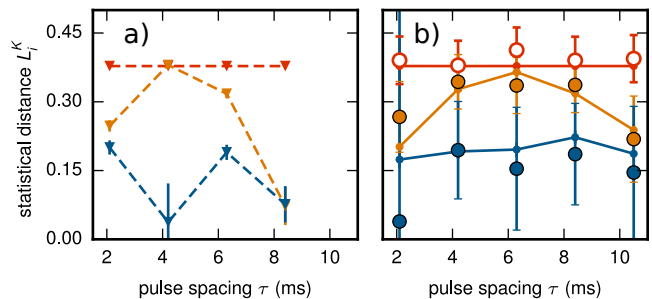


FIG. 4. Statistical distance between cooling pulses. **a)** Simulated statistical distances L_i^K from the K directed divergence for $i = 1, 2, 3$ (red, yellow, blue), in the harmonic trap for various pulse spacings. **b)** Measured statistical distance for the anharmonic trap (large points) and corresponding simulations. In both cases, thermalization is mainly achieved during the first two pulses for the optimal spacing, with nearly equal statistical distances. The hollow points include the numerical contribution of the directed divergence of the momentum distribution [41].

mization criterion. The K directed divergence $K(\rho_3||\rho_f)$ is shown for various pulse spacings: the triangles correspond to numerical simulations for a harmonic trap, while the large dots are the experimental results for the nonharmonic trap (the small dots are the related simulations [41]). We observe a vanishing minimum in the harmonic case at 4.2 ms which corresponds to a quarter of a trap period. In this situation, the optimal pulse duration is hence given by the time needed to switch position and momentum axes in phase-space. The state ρ_3 after the last Raman pulse is here equal to the target thermal state ρ_f , revealing perfect thermalization. The nonharmonic case is more involved. Owing to the nonlinearity of the trapping force, each atom has a different period which depends on the oscillation amplitude. A single oscillation period for the atomic cloud is consequently not defined. We experimentally find a minimum of the K directed divergence at 6.3 ms, in good agreement with the numerical simulations. The entropic distance to the target state ρ_f is reduced by almost a factor two at this point compared to the non-optimum protocols.

Figure 2b displays the results of the second optimization criterion. The oscillation amplitude $\Delta K = \max_t K(f_3(t)||f_f) - \min_t K(f_3(t)||f_f)$ after the last cooling pulse for a free evolution up to 9 ms is represented for different pulse spacings, both for the harmonic (triangles) and nonharmonic (dots) trapping potentials. We again observe a minimum at 4.2 ms for the simulated harmonic case and at 6.3 ms for the experimental nonharmonic potential, thus confirming the findings obtained with the first static condition. Figure 2c shows as an illustration the time evolution of the K directed divergence $K(f_3(t)||f_f)$ after each cooling pulse for the optimal spacing. No oscillations are seen for the initial thermal state

ρ_0 (black). These oscillations strongly increase after the first cooling pulse (red), exposing the nonthermal nature of state ρ_1 , before decreasing again for the states ρ_2 and ρ_3 after the application of each additional Raman pulse (orange and blue), before reaching a minimum for ρ_3 .

We may combine both optimization criteria to draw a map of the cooling process in the plane $(K, \Delta K)$, similar to the schematic picture of Fig 1a. In this representation, changes along the K -axis correspond to a decrease of the energy of the atomic cloud, while a decrease of the amplitude ΔK indicates a thermalization of the gas. This map is shown in Fig. 3a for the numerical simulations and in Fig. 3b for the experimental data. Figures 3c-d exhibit the overlap between the measured (blue bars) and simulated (blue lines) axial atom distributions after the last Raman pulse, as well as the simulated target distribution (green lines) for $\tau = 2.1$ ms, 6.3 ms and 10.5 ms. We observe an overlap of 75% for the optimal time of 6.3 ms, twice the value for the other two times.

The fact that we can experimentally deduce the axial phase-space distribution after each Raman pulse, and not just after the last one, allows us to gain physical insight on the whole cooling process by evaluating the statistical distance L_i associated with each cooling step. Figure 4a presents the simulated statistical distances L_i^K , ($i = 1, 2, 3$) based on the K directed divergence for the harmonic trap. We note that the first two steps (red and orange) have equal length for the optimal pulse spacing of 4.2 ms, while the length of the last step vanishes. Thermalization therefore occurs only during the first two Raman pulses. This picture is slightly modified for the nonharmonic potential (Fig. 4b). However, even in this instance, the data demonstrates that thermalization of the cloud is predominantly induced by the first two cooling pulses for the optimal pulse spacing of 6.3 ms.

We have experimentally optimized the cooling of a gas of noninteracting Cesium atoms by associating laser cooling techniques with nonequilibrium thermodynamics. Our findings demonstrate an effective method to thermalize nonharmonically trapped dilute gases. They further highlight the practical usefulness of nonequilibrium concepts such as entropy production and statistical distances down to the atomic level. They finally provide a versatile experimental platform to investigate more complex far from equilibrium optimization protocols including interacting particles in the quantum regime, as well as power output mechanisms and thermal machines [50].

[1] A. Bejan, *Advanced Engineering Thermodynamics*, (Wiley, New York, 2006).
 [2] P. Salamon and R. S. Berry, Thermodynamic Length and Dissipated Availability, *Phys. Rev. Lett.* **51**, 1127 (1983).
 [3] B. Andresen, P. Salamon, and R. S. Berry, Thermody-

namics in finite time, *Phys. Today* **37**, 62 (1984).
 [4] J. Nulton, P. Salamon, B. Andresen, and Qi Anmin, Quasistatic processes as step equilibrations, *J. Chem. Phys.* **83**, 334 (1985).
 [5] B. Andresen, Current Trends in Finite-Time Thermodynamics, *Angew. Chem., Int. Ed.* **50**, 2690 (2011).
 [6] P. Salamon and J.D. Nulton, The geometry of separation processes: A horse-carrot theorem for steady flow systems, *Europhys. Lett.* **42**, 571(1998).
 [7] J. D. Nulton and P. Salamon, Optimality in Multi-stage Operations with Asymptotically Vanishing Cost, *J. Non-Equilib. Thermodyn.* **27**, 271 (2002).
 [8] K. Sekimoto, *Stochastic Energetics*, (Springer, Berlin, 2010).
 [9] U. Seifert, Stochastic thermodynamics, fluctuation theorems, and molecular machines, *Rep. Prog. Phys.* **75**, 126001 (2012).
 [10] T. Schmiedl and U. Seifert, Optimal Finite-Time Processes In Stochastic Thermodynamics, *Phys. Rev. Lett.* **98**, 108301 (2007).
 [11] E. Aurell, C. Mejia-Monasterio, and P. Muratore-Ginanneschi, Optimal Protocols and Optimal Transport in Stochastic Thermodynamics, *Phys. Rev. Lett.* **106**, 250601 (2011).
 [12] G. M. Wang, E. M. Sevick, E. Mittag, D. J. Searles, and D. J. Evans, Experimental Demonstration of Violations of the Second Law of Thermodynamics for Small Systems and Short Time Scales, *Phys. Rev. Lett.* **89**, 050601 (2002).
 [13] D. M. Carberry, J. C. Reid, G. M. Wang, E. M. Sevick, D. J. Searles, and D. J. Evans, Fluctuations and Irreversibility: An Experimental Demonstration of a Second-Law-Like Theorem Using a Colloidal Particle Held in an Optical Trap, *Phys. Rev. Lett.* **92** 140601 (2004).
 [14] S. Schuler, T. Speck, C. Tietz, J. Wrachtrup, and U. Seifert, Experimental Test of the Fluctuation Theorem for a Driven Two-Level System with Time-Dependent Rates, *Phys. Rev. Lett.* **94**, 180602 (2005).
 [15] V. Blickle, T. Speck, L. Helden, U. Seifert, and C. Bechinger, Thermodynamics of a Colloidal Particle in a Time-Dependent Nonharmonic Potential, *Phys. Rev. Lett.* **96**, 070603 (2006).
 [16] F. Douarche, S. Joubaud, N. B. Garnier, A. Petrosyan, and S. Ciliberto, Work Fluctuation Theorems for Harmonic Oscillators *Phys. Rev. Lett.* **97**, 140603 (2006).
 [17] C. Tietz, S. Schuler, T. Speck, U. Seifert, and J. Wrachtrup, Measurement of Stochastic Entropy Production, *Phys. Rev. Lett.* **97**, 050602 (2006).
 [18] S. Ciliberto, R. Gomez-Solano, and A. Petrosyan, Fluctuations, Linear Response, and Currents in Out-of-Equilibrium Systems, *Annu. Rev. Condens. Matter Phys.* **4**, 235 (2013).
 [19] G.E. Crooks, Measuring thermodynamic length, *Phys. Rev. Lett.* **99**, 100602 (2007).
 [20] E. H. Feng and G.E. Crooks, Far-from-equilibrium measurements of thermodynamic length, *Phys. Rev. E* **79**, 012104 (2009).
 [21] D. A. Sivak, G. E. Crooks, Thermodynamic metrics and optimal paths, *Phys. Rev. Lett.* **108**, 190602 (2012).
 [22] T. R. Gingrich, G. M. Rotskoff, G. E. Crooks, P. L. Geissler, Near-optimal protocols in complex nonequilibrium transformations, *Proc. Natl. Acad. Sci. U.S.A.* **11**, 10263 (2016).
 [23] H. J. Metcalf and P. van der Straten, *Laser Cooling and*

- Trapping*, (Springer, Berlin, 1999).
- [24] C. Cohen-Tannoudji and D. Guery-Odelin, *Advances in Atomic Physics*, (World Scientific, Singapore, 2011).
- [25] V. Vuletic, C. Chin, A. J. Kerman, and S. Chu, Degenerate Raman Sideband Cooling of Trapped Cesium Atoms at Very High Atomic Densities, *Phys. Rev. Lett.* **81**, 5768 (1998).
- [26] A. J. Kerman, V. Vuletic, C. Chin, and S. Chu, Beyond Optical Molasses: 3D Raman Sideband Cooling of Atomic Cesium to High Phase-Space Density, *Phys. Rev. Lett.* **84**, 439 (2000).
- [27] D.-J. Han, S. Wolf, S. Oliver, C. McCormick, M. T. DePue, and D. S. Weiss, 3D Raman Sideband Cooling of Cesium Atoms at High Density, *Phys. Rev. Lett.* **85**, 724 (2000).
- [28] P. Treutlein, K. Y. Chung, and S. Chu, High-brightness atom source for atomic fountains, *Phys. Rev. A* **63**, 051401 (2001).
- [29] T. Weber, J. Herbig, M. Mark, H.-C. Nägerl, and R. Grimm, Bose-Einstein Condensation of Cesium, *Science* **299**, 232 (2003).
- [30] C. Monroe, D. M. Meekhof, B. E. King, S. R. Jefferts, W. M. Itano, D. J. Wineland, and P. Gould, Resolved-Sideband Raman Cooling of a Bound Atom to the 3D Zero-Point Energy, *Phys. Rev. Lett.* **75**, 4011 (1995).
- [31] L. Deslauriers, P. C. Haljan, P. J. Lee, K.-A. Brickman, B. B. Blinov, M. J. Madsen, and C. Monroe, Zero-point cooling and low heating of trapped $^{111}\text{Cd}^+$ ions, *Phys. Rev. A* **70**, 043408 (2004).
- [32] H. J. Lee, C. S. Adams, M. Kasevich, and S. Chu, Raman Cooling of Atoms in an Optical Dipole Trap, *Phys. Rev. Lett.* **76**, 2658 (1996).
- [33] L. W. Cheuk, M. A. Nichols, M. Okan, T. Gersdorf, V. V. Ramasesh, W. S. Bakr, T. Lompe, and M. W. Zwierlein, Quantum-Gas Microscope for Fermionic Atoms, *Phys. Rev. Lett.* **114**, 193001 (2015).
- [34] M. F. Parsons, F. Huber, A. Mazurenko, C. S. Chiu, W. Setiawan, K. Wooley-Brown, S. Blatt, and M. Greiner, Site-Resolved Imaging of Fermionic ^6Li in an Optical Lattice, *Phys. Rev. Lett.* **114**, 213002 (2015).
- [35] M. Gröbner, P. Weinmann, E. Kirilov, and H.-C. Nägerl, Degenerate Raman sideband cooling of ^{39}K , *Phys. Rev. A* **95**, 033412 (2017).
- [36] A. M. Kaufman, B. J. Lester, and C. A. Regal, Cooling a Single Atom in an Optical Tweezer to Its Quantum Ground State, *Phys. Rev. X* **2**, 041014 (2012).
- [37] J. D. Thompson, T. G. Tiecke, A. S. Zibrov, V. Vuletic, and M. D. Lukin, Coherence and Raman Sideband Cooling of a Single Atom in an Optical Tweezer, *Phys. Rev. Lett.* **110**, 133001 (2013).
- [38] F. Schmidt, D. Mayer, M. Hohmann, T. Lausch, F. Kindermann, and A. Widera, Precision measurement of the ^{87}Rb tune-out wavelength in the hyperfine ground state $F = 1$ at 790 nm, *Phys. Rev. A* **93**, 022507 (2016).
- [39] M. Hohmann, F. Kindermann, T. Lausch, D. Mayer, F. Schmidt, and A. Widera, Single-atom thermometer for ultracold gases, *Phys. Rev. A* **93**, 043607 (2016).
- [40] P. R. Bevington and D. K. Robinson, *Data Reduction and Error Analysis for the Physical Sciences* (McGraw-Hill, New York, 2003).
- [41] See Supplemental Material
- [42] D. Mayer, F. Schmidt, D. Adam, S. Haupt, J. Koch, T. Lausch, J. Nettersheim, Q. Bouton, and A. Widera, Controlled doping of a bosonic quantum gas with single neutral atoms, *J. Phys. B: At. Mol. Opt. Phys.* **52**, 015301 (2019).
- [43] G. Lebon, D. Jou, and J. Casas-Vásquez, *Understanding Non-Equilibrium Thermodynamics* (Springer, Berlin, 2008).
- [44] F. Schlögl, Stochastic Measures in nonequilibrium thermodynamics, *Phys. Rep.* **62**, 287 (1980).
- [45] M. Esposito, K. Lindenberg, and C. V. d. Broeck, Entropy production as correlation between system and reservoir, *New J. Phys.* **12**, 013013 (2010).
- [46] S. Deffner and E. Lutz, Nonequilibrium entropy production for open quantum systems, *Phys. Rev. Lett.* **107**, 140404 (2011).
- [47] J. Lin, Divergence Measures Based on the Shannon Entropy, *IEEE Trans. Inf. Theory*, **37**, 145 (1991).
- [48] T. M. Cover and J. A. Thomas, *Elements of Information Theory*, (Wiley, New York, 2006).
- [49] G. J. Milburn, Quantum and classical Liouville dynamics of the anharmonic oscillator, *Phys. Rev. A* **33**, 674 (1986).
- [50] J. Roßnagel, S. T. Dawkins, K. N. Tolazzi, O. Abah, E. Lutz, F. Schmidt-Kaler, and K. Singer, A single-atom heat engine, *Science* **352**, 325 (2016).

SUPPLEMENTAL MATERIAL

Numerical Simulations

For the numerical simulation of the phase-space dynamics in the DRSC protocols, the atomic motion in the trap is modeled with a Monte-Carlo approach where full trajectories of $N = 10^5$ atoms are calculated. This simulation only features two free parameters: First, the initial temperature of the atomic cloud T_0 determines the initial, thermal phase-space distribution, which sets the starting point for the simulation. Second, the Raman cooling temperature T_R is employed to model the effect of the DRSC by resetting the atomic velocities to a Maxwell-Boltzmann distribution corresponding to T_R , whenever a DRSC pulse is applied. Using these two temperatures together with precise information on the trap, the effect of arbitrary pulse sequences on the phase-space distribution and the ensuing dynamics can be computed. In this section, we show how the experimental value for T_0 is extracted from the measured initial distribution $f_0(z)$ and the Raman cooling temperature T_R is determined from the measured evolution after the first Raman cooling pulse $f_1(t, z)$.

In order to model the position distribution $f_0(z)$, we employ a simulation scenario, where atoms are initially located at the trap center. A heat bath at temperature T_0 is emulated by resetting the atomic velocities repeatedly to random velocities corresponding the desired initial temperature T_0 . Due to the resulting damped motion of the atoms in the trap, the atomic position distribution approaches a thermal distribution at T_0 [39]. We compare the simulated position distributions $f_{\text{sim}}(z)$ for various temperatures T_0 to the experimentally measured

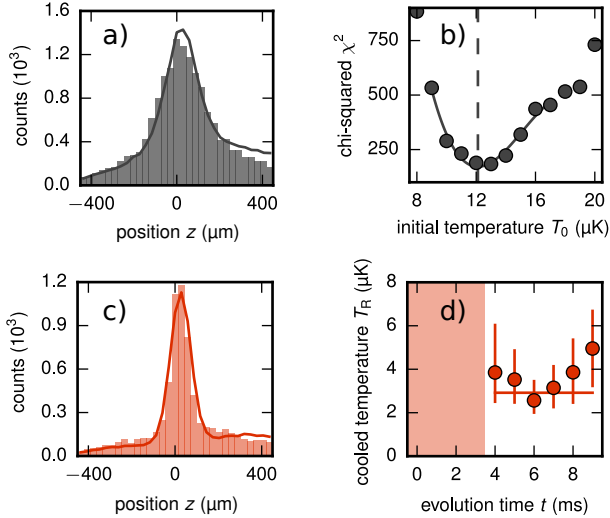


FIG. 5. Fitting of initial and final temperatures. a) Experimental position distribution (bars) and best fitting simulated distribution with $T_0 = 12 \mu\text{K}$ (solid line). b) The initial temperature is extracted by calculating the χ^2 -value for various initial temperatures (markers) and then using a polynomial fit around the minimum of the curve (solid line) to extract the best fitting temperature $T_0 = 12.1(11) \mu\text{K}$ (dashed line). c) Experimental position distribution after a single DRSC pulse and $t = 6 \text{ ms}$ evolution time (bars) and best fitting simulated distribution with $T_R = 3 \mu\text{K}$ (solid line). d) Applying a χ^2 -analysis for every evolution time t yields different cooled temperature estimates (markers). We extract the overall cooled temperature $T_R = 2.9(2) \mu\text{K}$ by employing a weighted fit (solid line).

initial position distribution $f_{\text{exp}}(z)$ shown in Fig. 5a by calculating the χ^2 -value,

$$\chi^2 = \sum_{z_i} \left(\frac{f_{\text{sim}}(z_i) - f_{\text{exp}}(z_i)}{\Delta f_{\text{sim}}(z_i) + \Delta f_{\text{exp}}(z_i)} \right)^2 \quad (2)$$

for the binned data as a measure for the goodness of the fit [40] (Δf_{sim} and Δf_{exp} are the statistical uncertainties of f_{sim} and f_{exp}). The χ^2 -value for simulations at various temperatures is shown in Fig. 5b, where we use a polynomial fit to the data in order to extract the initial temperature $T_0 = 12.1(11) \mu\text{K}$.

The final temperature T_R which corresponds to the DRSC temperature is not visible in the position distribution directly after a DRSC-pulse. However, as illustrated in Fig. 1d, the evolution in the trapping potential after the first DRSC pulse shows clear evidence of the cooling effect by featuring a breathing behavior. In order to extract the value of T_R , we simulate the time evolution of atomic samples which are prepared at the initial temperature T_0 and then reset the atomic velocities to values corresponding to different Raman cooling temperatures T_R . For every evolution time t , we extract

a Raman cooling temperature T_R with a χ^2 -analysis, analogous to the strategy employed for the initial distribution, by comparing the simulations for different Raman cooling temperatures to the experimental distribution (fig 5c). We combine the results of all measured evolution times shown in Fig. 5d by a weighted constant fit to the data, thereby extracting the DRSC temperature $T_R = 2.9(2) \mu\text{K}$. The red shaded area in the plot indicates small evolution times t where the χ^2 -analysis fails, because the information about the velocity distribution is not yet transformed into the position distribution. This behavior is also visible in the size of the error bars, which first decreases until $t = 6 \text{ ms}$ and then increases again.

Statistical distance

We begin by reminding the derivation of the entropy production for a single equilibration step [46]. We consider a system with Hamiltonian H in an initial state ρ_0 that thermalizes to the equilibrium state ρ_{eq} with inverse temperature β . The entropy production is defined as $\Sigma = \Delta S - \beta Q$, where $\Delta S = - \int dz dp_z (\rho_{\text{eq}} \ln \rho_{\text{eq}} - \rho_0 \ln \rho_0)$ is the entropy difference between final and initial states and $Q = \int dz dp_z H(\rho_{\text{eq}} - \rho_0)$ the corresponding heat. Using $\rho_{\text{eq}} = \exp(-\beta H)/Z$, one readily finds [44, 46],

$$\Sigma = D(\rho_0 || \rho_{\text{eq}}) = \int dz dp_z (\rho_0 \ln \rho_0 - \rho_0 \ln \rho_{\text{eq}}). \quad (3)$$

Let us now consider a multistep equilibration process with one intermediate (nonthermal) state ρ_1 . The entropy production between this state and the equilibrium state ρ_{eq} is $\Sigma_1 = D(\rho_1 || \rho_{\text{eq}})$. Using the additivity of the entropy production, $\Sigma = \Sigma_0 + \Sigma_1$, we obtain the entropy production between state ρ_0 and ρ_1 as [45, 46],

$$\Sigma_0 = D(\rho_0 || \rho_{\text{eq}}) - D(\rho_1 || \rho_{\text{eq}}). \quad (4)$$

We refer to Refs. [1, 2] for a recent alternative derivation. Expression (4) can be generalized to an arbitrary number of nonthermal intermediate steps by recursion, yielding,

$$\Sigma_i = D(\rho_i || \rho_{\text{eq}}) - D(\rho_{i+1} || \rho_{\text{eq}}). \quad (5)$$

The square root of Eq. (5), $L_i = \sqrt{2\Sigma_i}$, defines a statistical distance. Common optimization schemes consider thermal intermediate states generated by coupling the system to different baths at (slightly) different temperatures [4–7]. For such quasistatic transformation, the statistical distance reduces to the usual thermodynamic length [4–7].

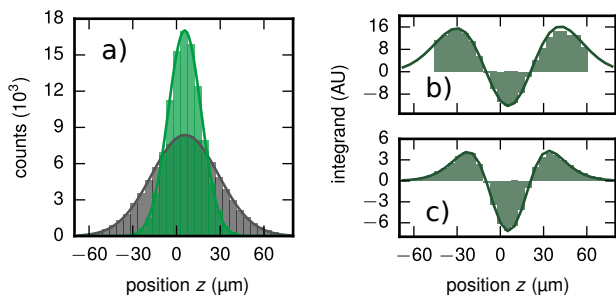


FIG. 6. Numerical calculation of the relative entropy. a) Monte-Carlo simulations for an initial distribution at $T_0 = 1 \mu\text{K}$ (gray bins) and a final distribution at $T_R = 0.25 \mu\text{K}$ (green bins). At these temperatures, the trapping potential is approximately harmonic, Gaussian distributions (solid lines) can thus be fitted to the Monte-Carlo results. b) Integrand \mathcal{D}_i for the calculation of the relative entropy $D(f_i||f_f)$. c) Integrand \mathcal{K}_i for the calculation of the directed divergence $K(f_i||f_f)$. Bins correspond to the calculation based on the Monte-Carlo data, while solid lines represent the integrands based on the fitted Gaussian distributions shown in a).

Numerical calculation of the relative entropy

For the analysis of our data, we typically bin the atomic positions from an experiment or a Monte-Carlo simulation in order to create a numerical representation of the density distribution. The integral for the relative entropy then corresponds to a sum over all bins z_i , where

$$D(f_1||f_2) = \sum_{z_i} f_1(z_i) \log \left(\frac{f_1(z_i)}{f_2(z_i)} \right) \delta z_i \quad (6)$$

$$= \sum_{z_i} \mathcal{D}_i \delta z_i. \quad (7)$$

As discussed in Ref. [47], typical data with finite statistics may exhibit bins where $f_2(z_i) = 0$, meaning that no atom has been observed in this bin. However, this corresponds to a division by zero in Eq. (6), rendering the calculation of the integrand value \mathcal{D}_i impossible for this specific bin. In contrast, the directed divergence [47],

$$K(f_1||f_2) = \sum_{z_i} f_1(z_i) \log \left(\frac{f_1(z_i)}{f_1(z_i) + f_2(z_i)} \right) \delta z_i \quad (8)$$

$$= \sum_{z_i} \mathcal{K}_i \delta z_i, \quad (9)$$

can be evaluated even at bins where $f_2(z_i) = 0$. It is therefore much more robust especially when analyzing experimental data, where statistical errors are usually even more pronounced.

In order to illustrate the problem, we employ the data set used for the harmonic approximations shown in Figs. 2 and 4. The corresponding initial temperature for the simulation is $T_0 = 1 \mu\text{K}$ and the final temperature

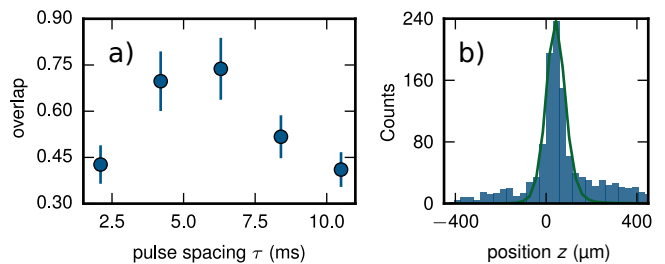


FIG. 7. Overlap calculation. a) The overlap of the distribution after the last cooling pulse $f_3(0)$ with the final distribution f_f shows a maximum at 6.3 ms in agreement with our optimization result. b) Illustration of the experimental distribution $f_3(0)$ for the optimum pulse spacing (blue bars) and the renormalized final distribution (green line).

is $T_R = 0.25 \mu\text{K}$. While these values are more than one order of magnitude colder than the experimental parameters, the ratio of the two temperatures is the same as in the experiment, thereby providing a comparable cooling process. Nevertheless, at these low temperatures, the harmonic approximation of the trapping potential holds also in axial direction. In fact, the density distributions of the Monte-Carlo simulation (bars) shown in Fig. 6a fit very well to Gaussian distributions (solid lines) which are expected for the harmonic case. Figures 6b and c show the integrands \mathcal{K}_i and \mathcal{D}_i , where again the bars correspond to the numerical data and the solid lines show the Gaussian fit. The missing bars seen in Fig. 6b clearly indicate the numerical problem connected to the relative entropy. By contrast, the integral for the directed divergence in Fig. 6c can be evaluated in the whole range.

Contributions of the momentum distribution

For factorized distributions $\rho_i = f_i(z)\tilde{f}_i(p_z)$ the relative entropy D can be split into two contributions $D(\rho_i||\rho_f) = D(f_i(z)||f_f(z)) + D(\tilde{f}_i(p_z)||\tilde{f}_f(p_z))$, where the first term accounts for the position distribution and the second takes into account the momentum distribution. After a Raman cooling pulse (for $i = 1, 2, 3$), the contribution of the momentum distributions is zero, because $f_i(p_z)$ and $f_f(p_z)$ are identical. For the initial distribution ($i = 0$), however, this contribution is not zero, as here the momentum distributions are not equal. In the measured position distributions $f_0(p_z)$ at $t = 0$, this contribution is not visible. However, as the initial (T_0) and final (T_R) temperatures are known, the contribution $D(\tilde{f}_0(p_z)||\tilde{f}_f(p_z))$ can be calculated from the thermal momentum distributions $\tilde{f}(p_z, T) = 1/\sqrt{2\pi mkT} \cdot \exp(-p_z^2/(2mkT))$. We find for the directed divergence employed in Figs. 3, 4 this contribution of the momen-

tum distribution to be $K(\tilde{f}(p_z, T_0) || \tilde{f}(p_z, T_R)) = 0.071$ by solving the integral numerically. The hollow experimental points in Figs. 3, 4 are thus a combination of the measured contribution to the directed divergence from the position distribution and the numerically deduced contribution from the momentum distribution.

Overlap calculation

The overlap of the distribution after the last cooling pulse $f_3(0)$ with the final distribution f_f is evaluated in the following way. We first renormalize the final distribution (green line) to the maximum of the experimental data (blue bars). Integration of the renormalized final

distribution then yields the amount of atoms in the experimental distribution that match the final distribution. We identify this value with the overlap. We find the largest overlap at a pulse spacing of 6.3ms which corresponds to our optimization result (Fig. 7).

-
- [1] S. Cusumano, V. Cavina, M. Keck, A. De Pasquale, and V. Giovannetti, Entropy production and asymptotic factorization via thermalization: A collisional model approach, *Phys. Rev. A* **98**, 032119 (2018).
 - [2] L. Mancino, V. Cavina, A. De Pasquale, M. Sbroscia, R. I. Booth, E. Roccia, I. Gianani, V. Giovannetti, and M. Barbieri, Geometrical Bounds on Irreversibility in Open Quantum Systems, *Phys. Rev. Lett.* **121**, 160602 (2018).